Journal of The Electrochemical Society, **157** (12) B1753-B1761 (2010)
0013-4651/2010/157(12)/B1753/9/$28.00 © The Electrochemical Society

Pore-Level Liquid Water Transport Through Composite Diffusion Media of PEMFC

Yan Ji, Gang Luo, and Chao-Yang Wang[*,z]

Electrochemical Engine Center and Department of Mechanical and Nuclear Engineering, The Pennsylvania State University, University Park, Pennsylvania 16802, USA

Liquid water transport at the pore level in a composite microporous layer (MPL) and carbon paper gas diffusion layer (GDL), used in a proton exchange membrane fuel cell (PEMFC), has been simulated for the first time by a topologically equivalent pore network (TEPN). Extracted from stochastic generated three-dimensional porous media that replicate typical patterns of void space and fiber connectivity observed in high resolution two-dimensional images of carbon paper GDL and a regular MPL made of carbon black and poly(tetrafluoroethylene), the TEPN for the composite diffusion media is used as input to an invasion percolation flow simulator. Steady-state liquid water distribution and saturation profiles in the MPL–GDL composite media are determined. In the interfacial region between the MPL and the GDL, liquid water saturation increases sharply due to a dramatic change in pore size, confirming the saturation discontinuity modeled in the continuum approach. The effects of current density and MPL thickness on liquid water saturation profiles are also explored. The results suggest that, in contrast to the MPL, liquid water saturation in the GDL is less affected by the current density. A thicker MPL helps to achieve a lower saturation level in the GDL by reducing the number of liquid injection sites into the GDL.
 [DOI: 10.1149/1.3491359]

Manuscript submitted July 1, 2010; revised manuscript received August 30, 2010. Published September 30, 2010.

Proton exchange membrane fuel cells (PEMFCs) hold promise as a next generation of power sources for portable and automobile applications due to their high energy density, low emission, low operation temperature, and low noise. The low operation temperature allows for fast startup; however, it incurs the presence of liquid water, which plays a conflicting role in PEMFC. Water hydrates the membrane and hence reduces its ohmic loss. However, high water content may cause flooding in the catalyst layer (CL), gas diffusion layer (GDL), and gas channels (GCs), thus incurring severe activation and concentration losses. Therefore, water management, calling for a delicate balance between membrane dehydration and electrode flooding, is crucial in optimizing the performance of PEMFC.

The GDL, which is made of nonwoven carbon paper or woven carbon cloth, is a highly porous medium that is designed to exhibit high electronic and thermal conductivity, low gas diffusion, and liquid transport resistances, as well as mechanical support to the CL. In the cathode side, oxygen diffuses from the GC across the GDL to reach the reaction sites, whereas water generated in the CL is also drained out through the GDL. At high current densities, the accumulation of excess water blocks the pores in the GDL and hinders the oxygen diffusion process, resulting in significant mass transport and performance losses. To avoid flooding, different treatments of the porous transport layers have been used. One typical way is to treat the GDL structure with hydrophobic materials, such as poly(tetrafluoroethylene) (PTFE) to change its wettability. Another method is to add a microporous layer (MPL) between the GDL and the CL.

The MPL is a mixture of carbon black and PTFE coated on a carbon paper substrate.[1] Compared with the GDL, whose mean pore radius is on the order of 10 μm, the MPL features a finer pore structure with mean pore radius on the order of 0.5 μm. Although adding an MPL improves the fuel cell performance by enhancing the contact and mechanical compatibility between sandwiched layers (lowering the ohmic loss)[2] and by assisting in the local distribution of oxygen and current density,[3] its effect in overall water transport has been a subject of debate in both theoretical modeling[2,4-6] and experimental studies.[7-11] The central issue here has been whether the cathode MPL enhances water back-diffusion through the membrane or increases water removal rate from the cathode CL to the GDL. With the growth of investigations on the MPL effect, especially the experimental database, the hydrophobic cathode MPL incurs the buildup in liquid pressure difference across the membrane, resulting in an enhanced rate of water back-flow to the anode and a reduced amount of water that flows into the cathode GDL. Back-diffusion hydrates the membrane and thus decreases the ohmic loss, whereas the reduced flooding in cathode GDL leads to lower mass transport limitation.

Numerous theoretical and numerical studies[2,4-6,11] have been conducted to understand the liquid water transport behavior in the diffusion media of PEMFC, following the macroscopic approach based on continuum two-phase Darcy's law. The macroscopic models require constitutive relations, such as capillary pressure and relative permeability, as functions of liquid water saturation. These relations are material-specific. The accurate prediction of these relations calls for the incorporation of the material microstructure. To understand the pore-level liquid water transport in the diffusion layers, mesoscopic approaches have been developed, such as the pore network model, the full morphology model,[12] and the lattice Boltzmann method,[13] to take into account of the material-specific microstructures. Among various mesoscopic approaches, the pore network model stands out owing to its low computational cost and clear reflection of the physics in the pore-scale liquid–vapor transport processes.

The pore network model was originally designed to study multiphase flow in soil and rocks, oil reservoirs, and hydrological formations. The use of the pore network model in the area of PEMFC started with Nam and Kaviany.[4] They determined the effective mass diffusivity in a fibrous GDL as a function of porosity and water saturation using a network of cubic cells. The first attempt by using a three-dimensional (3D) pore network to simulate liquid water transport in the GDL was realized by Sinha and Wang.[14] The liquid water transport at the pore scale was dynamically simulated in a hydrophobic GDL under realistic operation conditions. They showed a fingerlike liquid front that confirmed the capillary fingering regime for water transport in the GDL. Sinha and Wang[15] also studied the effect of mixed wet GDL on the liquid water transport. Liquid water preferentially flowed through hydrophilic pores and suppressed the fingerlike morphology to stable-front, which, however, supported the applicability of the two-phase Darcy's law. Markicevic et al.[16] investigated capillary pressure and relative permeability relations using a two-dimensional capillary network composed of uniformly distributed pores. Gostick et al.[17] used the regular cubic pore network that was calibrated to two GDL materials to obtain the material-specific relative permeability and diffusivity under quasi-static drainage conditions. Their results suggested that the commonly used constitutive relations in PEMFC may significantly overestimate the gas phase transport properties. Lee et al.[18,19] investigated water transport in the GDL represented by a randomly

* Electrochemical Society Active Member.
z E-mail: cxw31@psu.edu

Table I. Parameters for the composite MPL–GDL TEPN.

Parameter	GDL	MPL	Composite
Pore number	580	26,733	27,313
Throat number	2840	177,137	179,977
Cross-sectional area	300×300 μm^2	300×300 μm^2	300×300 μm^2
Through-plane thickness	200 μm	100 μm	300 μm
Porosity	0.73	0.24	—
Permeability	5.9×10^{-12} m^2	6.1×10^{-14} m^2	—

generated cubic network. Their results showed that liquid water transport in hydrophobic GDL almost reached the pure invasion percolation limit with zero capillary number, and the saturation profiles were characterized by a concave shape. The effect of the inlet condition and GDL thickness were also investigated. Rebai and Prat[20] investigated the scale effect in a hydrophobic GDL and concluded that the lack of length scale separation between pore scale and GDL thickness leads to the poor prediction of the macroscale approach. Their calculations indicated that both the capillary pressure and relative permeability were dependent on the GDL thickness. Ceballos and Prat[21] investigated the density of breakthrough pores as a function of porous layer thickness (either GDL or MPL).

However, all of the aforementioned studies employ randomly generated pore networks (RPNs), in which the cubic pores are placed on a 3D Cartesian grid such that each pore has six connections to its neighbors through throats with square cross sections. The radius of the pores and throats is randomly assigned in a range following a certain statistic distribution. In some studies, the pores are moved in random directions with a random distance to better reflect the disorderly distributed void spaces in the real porous media.

The RPN models are able to predict the capillary fingering process and fingerlike water morphology in porous layers of PEMFC. However, it employs randomly generated cubic pore network structures created to match average properties of GDL materials, such as porosity and permeability, which are insufficient to define a unique pore structure due to the lack of material-oriented microstructure information. Therefore, these pore network models lack the potential to delineate the effect of GDL pore structures on liquid water transport. Thompson[22] proposed a technique to generate prototype fibrous network structures from Voronoi diagrams, which is constructed around a set of random or disordered points. Although Voronoi diagrams are able to generate fibrous structures, they are random in nature and thus cannot replicate real materials.

To address this problem, we have recently developed a topologically equivalent pore network (TEPN) approach from high resolution GDL microstructures to realistically account for the profound influences of pore structures on water transport in the GDL and its associated constitutive relations.[23] The TEPN takes account of all material structural features and has the advantage to study the structure–performance relationship of diffusion media. The microstructures that differentiate carbon paper and carbon cloth materials are reflected in such aspects as pore- and throat-size distributions, nonuniform coordination number (defined as the number of throats connected to a pore), and nonuniform shape factor (different from spheres). By using TEPN, different effects of carbon paper and carbon cloth microstructure on liquid water transport behavior have been observed.[23]

Most recently, Gostick et al.[24] have studied the MPL effect by constructing a pore network model. The MPL is treated as a single layer with virtual nodes using continuum approximation. The pore-level water transport in the MPL cannot be captured by their model. Ceballos and Prat[21] investigated the ratio of breakthrough pore number to injection pore number in both the MPL and the GDL. However, the two porous layers are treated as two separated cubic pore networks. No work has existed to examine pore-scale water transport in MPL–GDL composite media, which are the most common case in PEMFC. A saturation jump exists at the interface between two porous media with different capillary properties. Macroscopic approaches attribute this behavior to the requirement in continuity of capillary pressure. How does this behavior manifest at pore level? To resolve this fundamental issue, the pore-level liquid water transport in a composite MPL–GDL structure is desired.

The objective of the present study is to shed light on the above problem by constructing a TEPN representing a composite MPL–GDL and to subsequently simulate the liquid water transport at PEMFC operating conditions. More fundamentally, this paper seeks to elucidate the saturation discontinuities at the MPL–GDL interface from the pore-level point of view. In addition, the effects of the current density and the MPL thickness on macroscopically averaged water saturation profiles are investigated.

Pore Network Model

A pore network model developed to study multiphase transport in porous media represents the large void spaces by pores and the narrow openings interconnecting the pores by throats. In PEMFC, the GDL is made of nonwoven carbon paper or woven carbon cloth both of which are porous materials with high porosity. By constructing the pore network to mimic the microstructure of a GDL, pore network models have been successfully employed to investigate the liquid water transport in the GDL of PEMFC.[14,15,18-21]

In the present study, the original microstructures of carbon paper GDL and MPL made of carbon powders and PTFE are constructed by using a stochastic simulation technique based on their high resolution two-dimensional images. The constructed microstructure of the composite is then processed by an imaging analysis to form a network of pores and throats. For a detailed description of the TEPN generation process, readers may refer to Ref. 23. Key parameters of this TEPN are summarized in Table I. Because MPL is included in the TEPN, despite a lower porosity, the small MPL pore size renders an increased number of pores by a factor of 10.[2] This large-scale pore network poses a great challenge to the memory requirement of the pore network generator as well as the computational cost to simulate the capillary invading process. To reduce the scale of the pore network, we have selected a cross-sectional area of 300×300 μm^2 for TEPN simulations.

A schematic plot of the composite TEPN is shown in Fig. 1. The MPL of thickness 100 μm is located at the bottom, whereas the GDL of 200 μm in thickness sits on the top. To form a better view, the pores, though irregular, are depicted as their largest inscribed spheres in Fig. 1. These spheres are plotted using the real size relative to the whole frame. For simplicity, we use black lines to represent the throats, whose size, however, is not reflected in the present figure.

The pore-size distributions of the composite TEPN are plotted in Fig. 2. Bimodal distributions can be seen: One primary mode with a higher peak represents the large GDL pores, whereas the other primary mode with a lower wide peak is associated with the MPL pores. The characteristic radius of the GDL pores is $\sim$10 μm, which is 1 order of magnitude higher than that of the MPL pores (1 μm). Between the two primary modes are the small pores in the GDL. The throat-radius distribution exhibits a similar trend as shown in Fig. 3, where the two primary modes are shown. However,

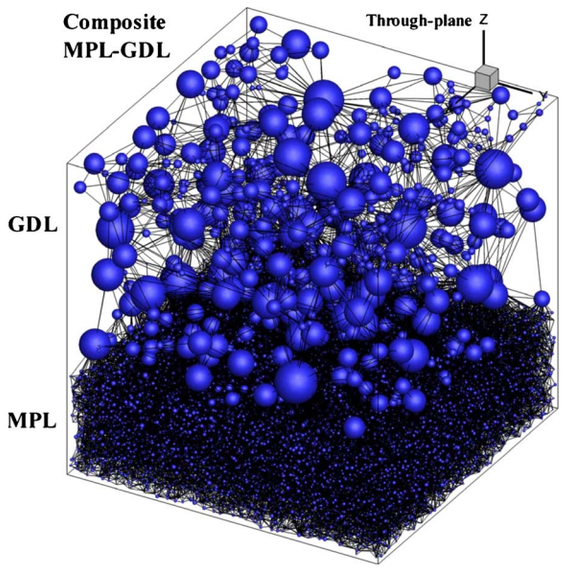

Figure 1. (Color online) Topologically equivalent pore network of the composite MPL–GDL.

this distribution shifts toward the left compared with the pore-size distribution, reflecting the fact that the throat radius is smaller than the pore radius on average.

Figure 4 provides a statistical view of the variation in the pore radius in the through-plane direction. The whole plot consists of

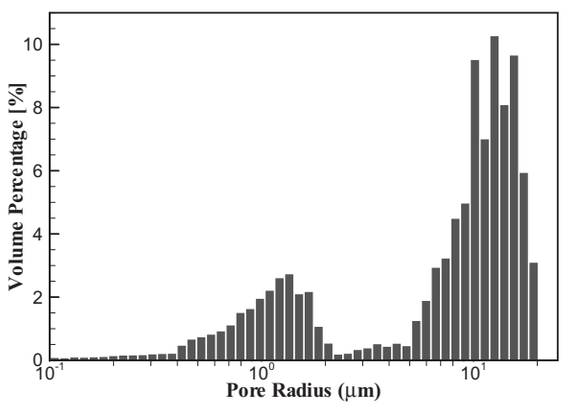

Figure 2. Pore-size distribution of the composite MPL–GDL structure.

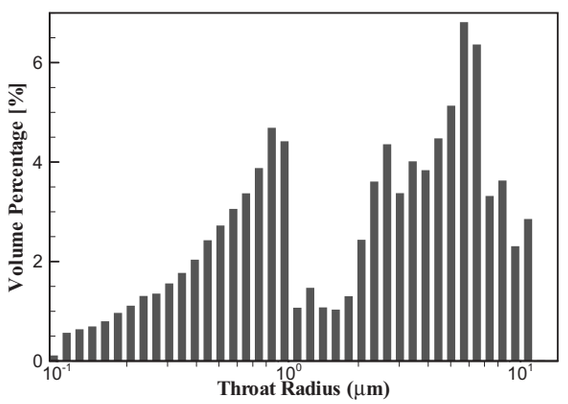

Figure 3. Throat-radius distribution of the composite MPL–GDL structure.

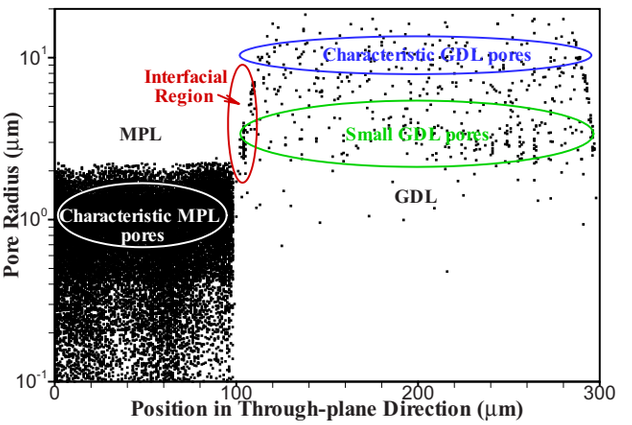

Figure 4. (Color online) Scatter plot of pore radius vs its through-plane position.

many tiny square dots. Each dot represents a pore whose location is indicated by the horizontal axis and whose radius is denoted by the vertical axis. The region with the densest dots marked by a white ellipse represents the characteristic MPL pores whose size distribution is shown in Fig. 2. The GDL characteristic pores are marked by the topmost ellipse. The pores in this region are much sparser yet much greater than the MPL pores, making them a primary mode based on the volume weighted percentage. Also marked here is the region consisting of the small GDL pores, most of which are still greater than the MPL pores.

As shown in Fig. 4, the MPL pores extend to a surface distinctly located approximately at 100 μm (more precisely 98–99 μm) in the through-plane position. However, the characteristic GDL pores start at the location ~110 μm. These two staggered locations create a gap between them, as indicated by the vertically extended ellipse. The width of the gap (11–12 μm) is roughly the sum of the radius of the GDL characteristic pore (10 μm) and MPL characteristic pore (1 μm) because the GDL and the MPL do not intrude into each other in the present TEPN. We call this gap the interfacial region, which is actually not a gap but filled continuously by those small GDL pores because their radii ranges between 1 and 10 μm. This interfacial region smooths the pore-size transition at the MPL–GDL interface. It is expected that this interfacial region affects the local capillary pressure and the liquid water saturation distribution, as discussed later.

Calculation of Liquid Water Invasion

The composite MPL–GDL TEPN has an overwhelming number of pores and throats, as listed in Table I. The amount of MPL pores and throats are ~2 orders of magnitude greater than that in the GDL. As a comparison, the previous pore network studies of a single GDL comprises 4000 pores for the RPN[19] and only 2500 pores for the TEPN.[19] To reduce the computational cost for liquid water transport in this composite TEPN with high degrees of freedom, we devised a simplified invasion percolation algorithm.

The water transport in the MPL–GDL is a drainage process (displacement of the wetting phase by the nonwetting phase) because liquid water is the nonwetting phase here, with the assumption of the fully hydrophobic MPL–GDL. Based on the phase diagram[25] for the two-phase drainage process, the regime of the immiscible displacement depends on the capillary number (Ca) and viscosity ratio (M). For a typical PEMFC operation, the viscosity ratio is 17.5 and the capillary number is on the order of 10^{-8}.[14] The two-phase flow in the MPL–GDL falls in the capillary fingering regime. Due to the extremely small Ca, the invasion process reaches a limit that is almost fully controlled by capillary forces. The validity of this conclusion is examined by previous studies.[14,18,19] We take advantage of

this invasion property by neglecting the viscous drop of the liquid pressure. This simplification eliminates the requirement of solving a system of equations for liquid pressure at each step, thus greatly reducing the computational cost of pore network modeling in the composite structure. This simplification also enable us to make use of the invasion percolation algorithm,[26] which states that the liquid water advances at the interface at the point of least resistance. The rule of least resistance declares the invading priority of all the throats that have connections with a specific liquid cluster: The throat with the smallest capillary entry pressure possesses the highest invading priority.

In present calculations, a constant liquid flow rate equivalent to 1 A/cm^2 current density is specified at the inlet face of the MPL. In contrast to the uniform inlet pressure boundary condition under which only one liquid cluster can be formed, the uniform flux condition allows multiple liquid water clusters to coexist in the diffusion media. The invasion process stops until all the liquid clusters have access to the GC, yielding multiple breakthroughs at the GDL–GC interface, which agrees with experimental observations.[27] The uniform water injection rate condition has been employed in several recent pore network modeling studies.[18,19,24] A constant pressure boundary condition is set at the outlet surface open to the GC. All the lateral surfaces are subjected to the no-flow boundary condition.

The invasion process starts with injecting liquid water into the inlet throats at the CL–MPL interface. The ratio of the inlet throats injected by liquid water to the number of total throats at the inlet face is defined as the injection percentage ranging between 0 and 100%. For simplicity, we assume each injected throat shares the same portion of the total liquid flow rate. During the invasion process, each pore stays in one of the three statuses: invaded/flooded, invading, and uninvaded, in which invading means that liquid water invades an air filled pore with an advancing liquid–air interface. At the beginning of the invasion, each injected throat forms an independent liquid water cluster. All the liquid clusters are invaded simultaneously. The time step is chosen such that only one pore is completely invaded in each time interval. At the end of each step, the next invading pore is searched from a pool of candidate pores according to the rule of least resistance for all the throats connected to the corresponding cluster. Six possible situations may be encountered here:

1. The next invading pore was originally an air filled pore. Then, the corresponding liquid cluster grows independently by invading that pore.
2. The next invading pore was an invaded pore in the same cluster. In this case, only the throat connecting the next invading pore is invaded. A new invading pore needs to be identified for this cluster.
3. The next invading pore is an invaded pore in a different cluster. Then, the two clusters merge to form one cluster. The liquid invasion rate for this new cluster is the sum of the 2 original clusters. This updated liquid flow rate is used for invasion of the presently invading pore.
4. The next invading pore is also an invading pore but belongs to a different cluster. The two clusters merge to form one cluster once this invading pore is completely flooded.
5. The next invading pore is located at the outlet. Then, a breakthrough is formed at the GDL–GC interface. The growth of this cluster stops.
6. The next invading pore locates in a cluster that already has access to the outlet. The two clusters merge but do not grow.

The above six cases cover all possible situations at the end of each time step. The whole invasion percolation process is a consequence of a series of quasi-steady steps. It advances step by step until all the liquid clusters have access (breakthrough) to the outlet.

At the beginning of invasion, the number of the invading pores is equal to the number of water clusters. During the invasion process, a gradual reduction of the invading pores occurs either by merging different liquid clusters or by achieving a breakthrough to the GC. No invading pore exists at the end of the invasion process. Despite the quasi-static process, the invasion time at any stage of the invasion is calculated by the liquid injection rates and the total volume of the flooded pores.

Due to the dominance of capillary force in the diffusion media of PEMFC, the liquid water morphology is controlled by both capillary pressure in the throats (throat entry pressure) and the material microstructure morphology. The microstructure is a crucial factor that affects liquid water distribution. From this view point, the TEPN is superior to the RPN in that it describes a more realistic pore structure that clearly differentiates different GDLs. In the TEPN, pores and throats have irregular shapes that are described by a shape factor. The shape factor of a throat is defined as the ratio of cross-sectional area to the squared perimeter[28]

$$G = A/P^2 \quad [1]$$

Then the throat entry pressure is given by

$$p_c = \sigma \frac{1 + 2\sqrt{\pi G}}{r} \cos\ \theta \quad [2]$$

where r is the throat largest inscribed radius and θ is the contact angle of the wetting phase (air). Despite that the viscous effect is neglected during the invasion process, the liquid pressure distribution is calculated at the end of capillary invasion. The calculation integrates the viscous resistance of the throats by assigning the flow conductance to the throats. We assume constant air pressure in the TEPN, considering that air in all the pores and throats are interconnected due to the small interstitial spaces where liquid water cannot reach. In saturated pores and throats, liquid water stays in the center and air locates in the corners. Thus, two-phase throat conductivity is affected by the area that a specific phase occupies. The liquid conductivity of a throat is calculated as

$$g_l = \frac{R_l^2 A_l}{8\mu_l L} \quad [3]$$

where A_l and R_l are calculated as

$$A_l = \frac{r^2}{4G}\left(\frac{\sigma}{r p_c}\right)^2 (1 - 4\pi G) \quad [4]$$

$$R_l = \frac{r + \sqrt{A_l/\pi}}{2} \quad [5]$$

in which r, L, G, and p_c are throat radius, throat length, shape factor, and entry pressure, respectively. The liquid pressure is solved by using the mass conservation equation (assuming constant liquid density). For a saturated pore j, the total volume flow rate into this pore is zero

$$\sum_i Q_{ij} = G_{ij}(p_i - p_j) = 0 \quad [6]$$

Applying Eq. 6 to all the saturated pores constitutes a system of linear equations. By employing a linear solver, the liquid pressure distribution as well as the liquid flow rate in each throat is obtained.

At the end of the liquid water invasion calculation, liquid water saturation as a function of the through-plane position is computed. This saturation is a macroscopic property because it is an averaged value over a cross-sectional area that contains a large number of pores. Theoretically, the cross-sectional area possesses infinitesimal thickness. However, in the pore network model, we typically use a thin slice to represent the cross-sectional area. The thin slice is actually a representative element volume, over which the saturation is averaged as the ratio of the liquid occupied volume to the total void space. In the random pore network, despite that the pores are moved in random directions with random distances, they are roughly located layer by layer. To let each slice contain one layer of pores, the slice thickness is the distance between two adjacent pores. Thus, the

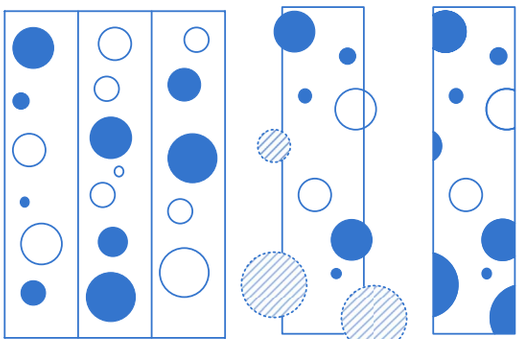

Figure 5. (Color online) Schematic of calculating macroscopic saturation. [Filled circles represent invaded pores. In (b), circles with solid edges and solid fills represent pores that are within the slice; circles with dashed edges and stripes inside represent pores that are not in the slice.]

slice is thick enough to allow us to simply use the center of a pore to decide it belongs to that layer, as shown in Fig. 5a. However, in TEPN, the location of pores depends on the material-specific structure. In the present TEPN, both MPL and GDL pores are distributed in a more randomized manner. If we still use that method, we miss many pores whose centers are outside the slice but still occupy a large portion of the void space, such as the partial filled pores with dashed edges shown in Fig. 5b. The extreme case for a thin slice is that none of the pore centers is located in the slice, whose saturation cannot be determined. This problem leads to a high sensitivity of saturation profile to the slice thickness. To solve this issue, we devise a method that accounts for any portion of pores in a slice, as shown in Fig. 5c. This improved method allows for slices that are thinner than the pore diameter. It also allows us to locate the slice at any through-plane position of the TEPN.

Results and Discussion

The following simulations have been performed only on one realization of the composite TEPN. Although statistically averaged results from many realizations are desired, the present one realization is intended to shed fundamental light on the physics at pore level.

Liquid water transport behavior in the composite MPL–GDL.— Despite the quasi-static nature of the present algorithm, the concept of time is used here along with the composite averaged saturation to mark the stage of the invasion percolation. The value of time is obtained by calculating the ratio of the saturated volume to the inlet liquid water injection rate. The liquid water paths at six time instants of the invasion process are shown in Fig. 6 from $t = 20$ s to the end of the invasion $t = 350$ s. In this investigation, all the inlet throats are injected by liquid water, leading to 100% injection percentage. Owing to the small size of the MPL pores, the inlet plane of the MPL has as much as 1979 throats. Accordingly, the initial number of the liquid water clusters is also 1979, which, however, drops rapidly due to the merge of liquid clusters with their growth. Here, we trace the growth of three clusters that are marked by red, green, and blue, respectively. All the other clusters are marked by yellow.

The liquid water distribution in Fig. 6 is an indication of the capillary fingering regime of the two-phase transport in the composite structure, which is characterized by the following behaviors: (*i*) The liquid cluster in the MPL grows in both the through-plane and spanwise directions as a result of capillary invasion and merging with other clusters. (*ii*) Once a liquid cluster reaches the GDL, its invasion in the MPL stops. The growth of this cluster continues either by invading GDL pores or merging with other clusters. For instance, the growth of the green cluster from $t = 60$ s to $t = 202$ s or the blue cluster from $t = 124$ s to the end of the invasion are observed only in the GDL. The cluster morphology in the MPL does not change. This behavior is a result of the much lower entry pressures of the GDL due to its coarser structure and wider throats. After reaching the GDL, the blue cluster grows independently by invasion, whereas the growth of green and red clusters is developed by both invasion and merging with other clusters.

The saturation discontinuity across the MPL–GDL interface.— A saturation discontinuity forms if a fine and a coarse porous media are brought together.[4,11,29] The liquid would redistribute as required by the continuity in capillary pressure. The saturation dis-

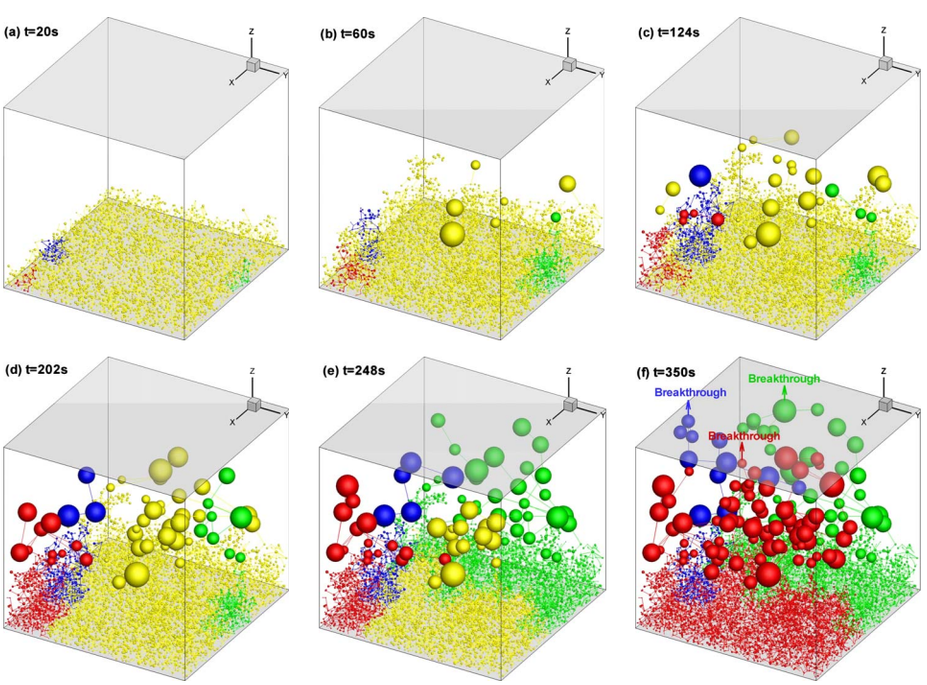

Figure 6. (Color online) Evolution of liquid water invasion in the composite TEPN. (Red, blue, and green represent three independent liquid clusters. Yellow represents all other liquid clusters).

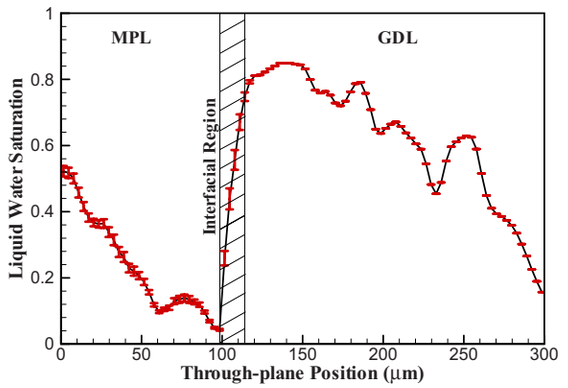

Figure 7. (Color online) Water saturation profile along the through-plane direction.

continuity can be predicted by using the continuum model based on the capillary pressure constitutive relations of the two porous media. In PEMFC, the MPL is a much finer porous medium whose pore sizes are at least 1 order of magnitude smaller than the GDL pores. It is therefore expected that a saturation jump exists at the MPL–GDL interface.[2,6] The saturation variation along the through-plane direction is readily attainable from the present TEPN simulations, as shown in Fig. 7.

Considering that oxygen needs to diffuse into the CL as the reactant, the inlet plane of the MPL is not completely flooded. The corresponding injection percentage is less than unity. A portion of inlet throats/pores are randomly selected as the liquid water pathways. The invasion percolation process is simulated for each set of random selection. To obtain a statistically averaged result, 100 selections of injection throats/pores are made at a specific injection percentage. 10% injection percentage is used here.

The water saturation profile is shown in Fig. 7, where the scattered error bars indicate the standard deviation of the saturation level computed from 100 selections of injection throats. The saturation in the MPL experiences a decrease from 0.52 at the CL–MPL surface to 0.04 and then followed by a sharp increase across the thin MPL–GDL interfacial region. The saturation continues to decrease in the GDL from the peak value 0.85–0.16 at the GDL–GC surface. The saturation profile is neither concave nor convex. It consists of many small rising ups and dropping downs, especially in the GDL component. This behavior is due to the limited number of (only one) realizations of the TEPN, as well as the fewer GDL pores that lead to larger standard deviation of the saturation.

Figure 7 indicates that the saturation discontinuity predicted by the present pore-level modeling is actually a sharp saturation increase from the MPL to the GDL across the thin interfacial region, which is also illustrated in Fig. 4. In the present TEPN without the intrusion of the MPL to the GDL, the interfacial region is a transition area caused by the small pores in the GDL, whose sizes are distributed between MPL pores (1 μm) and large GDL pores (10 μm). The thickness of this region is comparable to the size of the large GDL pores. After this region, the large pores in the GDL play a dominant role, leading to the highest level of the saturation. In practical applications, due to the compression among the membrane electrode assembly and porous layers, a portion of the MPL structure may intrude into the GDL. It is expected that the mix of the MPL pores and small GDL pores creates a much smoother transition region and hence a gentler increase in the saturation.

Instead of using the capillary pressure as a function of the saturation relation, from the pore-level point of view, the saturation jump can be explained from two aspects. For a clear illustration, we plot a schematic view of the porous layer microstructure at the MPL–GDL interface where filled pores and throats represent the status of being invaded, as shown in Fig. 8. The three vertical

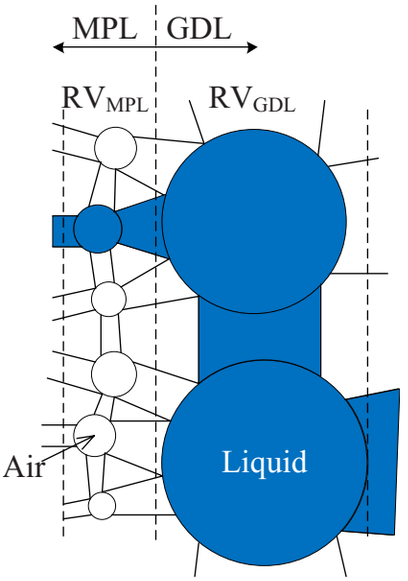

Figure 8. (Color online) A schematic view of the microstructure at MPL–GDL interface.

dashed lines create two slices. The left slice is actually a representative volume (RV) in the MPL (RV_{MPL}) and the right one is an RV in the GDL (RV_{GDL}). The RV is used here because we need to relate the pore-level liquid water distribution to the macroscopic saturation, which is defined as

$$s = \sum_{i \in RV} V_{pi} s_{pi} / \sum_{i \in RV} V_{pi} \qquad [7]$$

Here, V_{pi} represents the volume of pore i and s_{pi} is the pore-level saturation defined as the fraction of the void space occupied by liquid water in a pore.

In the first case, a liquid water cluster that has already reached the GDL preferentially invades GDL pores and is less likely to make further invasion in the MPL. This behavior is already seen in Fig. 6 and has been illustrated there. As also shown in Fig. 8, the GDL pores are connected by much wider throats with lower entry pressure. According to the least resistance principle, further invasion continues in the GDL and spread in the in-plane and channel directions, leading to higher macroscopic saturation in the RV_{GDL}.

In the second case, each GDL pore is connected to multiple MPL pores due to the large difference in pore size. The invasion into a GDL pore requires only one of its connected MPL pores being invaded. This multiple-to-one connection structure significantly increases the probability of invasion into the GDL and further reduces the macroscopic saturation in the RV_{MPL}.

Both of these factors are in favor of the higher saturation level in the GDL and lower saturation level in the MPL near the interfacial region. It is the combination of the two factors that creates a sharp rise of the liquid water saturation across a thin interfacial region (from 0.04 to 0.85). Considering that this result is from one realization of the TEPN, more realizations are needed to obtain a statistically averaged result based on which the saturation level on the two sides of the interfacial region can be related and compared with the predictions from the continuum model.

Effect of current density.— The injection percentage is the ratio of the number of throats/pores that are injected by liquid water to the total number of throats/pores at the inlet surface of the MPL (CL–MPL interface). This roughly reflects the percentage of the injection area where liquid water is injected with constant flow rate.

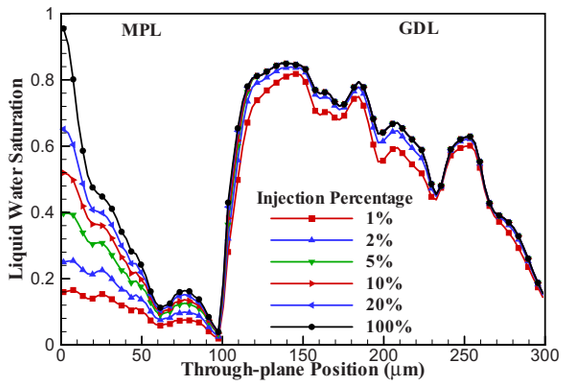

Figure 9. (Color online) Effect of injection percentage on liquid water saturation for MPL thickness of 100 μm.

The injection percentage is determined by the number of liquid water breakthroughs from the CL and the microstructure at the CL–MPL interface.

Based on catalyst agglomerate models, Nam et al.[29] estimated the density of the water breakthroughs at the CL surface. The upper limit density is calculated assuming liquid water is generated at each agglomerate particle. The agglomerate size is reported to be ~1 to 5 μm based on the scanning electron microscope micrographs.[30] For an average particle size of 3 μm, this estimation yields 1/9 μm^{-2} breakthroughs at the CL surface. The in situ observation[31] of water droplet formation at the CL surface gives a breakthrough density of 1/500 μm^{-2},[29] which is equivalent to the flooding probability of 1.8% for a CL surface pore. To obtain the injection percentage at the MPL inlet surface, an estimation of the flooding probability of the MPL surface pore is needed. In our TEPN, the 300 × 300 μm^2 inlet surface is covered by 1979 inlet throats. Each MPL inlet pore/throat occupies an area of ~45 μm^2, which contains five CL surface pores on the average. Assuming that liquid water breakthroughs from any of the five CL surface pores leads to the flooding of the corresponding MPL pore, which is reasonable due to the higher capillary pressure in the CL, the flooding probability of the MPL pore is calculated from a simple probability rule. (Nam et al.[29] used the same approach to estimate the flooding probability.)

$$1 - P_{f,MPL} = (1 - P_{f,CL})^N \quad [8]$$

which gives 8.8% injection percentage corresponding to the experimental observation. The injection percentage here is much less than unity. The above analysis demonstrates that the investigation on the injection percentage is significant. The injection percentage is controlled by the CL/MPL surface pore sizes and the flooding probability of CL surface pores, the latter of which is highly affected by the current density. The injection percentage is thus indicative of the current density. This investigation is helpful to examine the saturation level at low/high current densities.

The liquid water saturation profiles at different injection percentages are plotted in Fig. 9. Distinct saturation levels in MPL are clearly observed at different injection percentages. The level of inlet saturation is much higher than the injection percentage (such as inlet saturation of 0.16 for 1% injection percentage) owing to capillary invasion in the in-plane and channel directions. With the liquid water front advancement in the through-plane direction, saturation profiles of different injection percentages almost reach the same lowest level (ranging between 0.019 and 0.039) just before the MPL–GDL interfacial region. In the GDL, however, the saturation profiles cannot be differentiated except for the two cases with the lowest injection percentages (1 and 2%). Even for these two cases with very low injection percentages, saturation profiles are very close to others with higher injection percentages. The whole plot indicates that the saturation sensitivity to injection percentages is high in the MPL but extremely low in the GDL. Because the injection percentage is an indirect reflection of the current density, it is expected that, for low and high current densities, the saturation in the GDL almost remains at the same level despite very different saturation levels in the MPL.

Table II. Inlet condition at different MPL thicknesses.

MPL thickness (μm)	Inlet pore no.	Each inlet pore ~no. of CL agglomerates	Flooding probability (%)
100	1979	5.1	8.8
75	2193	4.6	8.0
50	2604	3.8	6.7
25	2145	4.7	8.2
0	110	90.9	80.8

In the invasion percolation process, the liquid water invasion paths are dictated by the inlet condition and the microstructure but not affected by the outlet condition. The liquid water path in the coarse GDL located in the downstream location is therefore only affected by its structure and the liquid water breakthrough locations and number from the MPL. Consequently, the GDL saturation behavior is actually a result of the saturation jump across the interfacial region. This sharp increase in saturation occurs even if the saturation level in the MPL is very low, as is due to the two factors that lead to the saturation jump mentioned in the last section.

This GDL saturation behavior is somewhat different from the recent experimental observations,[32,33] in which the cathode GDL water volume fraction profiles are distinct at different current densities. However, the present TEPN model is under isothermal condition with the assumption of a fully hydrophobic GDL and an ideal contact between the MPL and the GDL. The liquid water saturation in an operating GDL is influenced by a couple of effects in addition to the invasion percolation process, including evaporation and condensation, mixed wettability, as well as the contact condition between the MPL and the GDL. For example, in Hickner's in situ high resolution neutron experiments,[33] the drastic drop of water content from 0.75 to 1.00 A/cm^2 for 80°C cell temperature is attributed to the dominance of evaporation in the water removal process.

Effect of MPL thickness.— The water management role of MPL is studied by investigating its thickness effect. Without generation of a new TEPN, the present TEPN is cut by a flat virtual plane that is perpendicular to the through-plane direction. In this way, four sub-TEPN structures are generated, representing MPL thicknesses of 75, 50, 25, and 0 μm (GDL only), respectively. The GDL thickness is maintained the same. The injection percentages are selected to match the number of breakthrough pores emerging from the CL. Here, we use 1/500 μm^{-2} breakthrough density estimated from the in situ observation.[29,31] As shown in the last section, by using a simple probability relation (Eq. 8), the injection percentage is calculated based on the flooding probability of the CL surface pore and the average area taken by each MPL surface pore. We use the same method here and obtain the following inlet injection percentages, as shown in Table II. The much higher injection percentage of the GDL without the presence of the MPL is attributed to its relatively large pore size that increases surface pore flooding probability.

Due to the random selection of the inlet injected pores, 100 realizations are performed for each MPL thickness. The saturation profiles at different MPL thicknesses are plotted in Fig. 10. Each saturation profile is an average of the saturation distributions from 100 selections of injected pores.

Figure 10 indicates that adding an MPL between the CL and the GDL helps reduce the liquid water saturation level in the GDL, and a thicker MPL leads to a lower GDL saturation. This can be found by examination of the number of liquid water breakthroughs from the MPL, as shown in Table III. For a single GDL, the liquid breakthrough number from the CL is 89. After the MPL is added, the

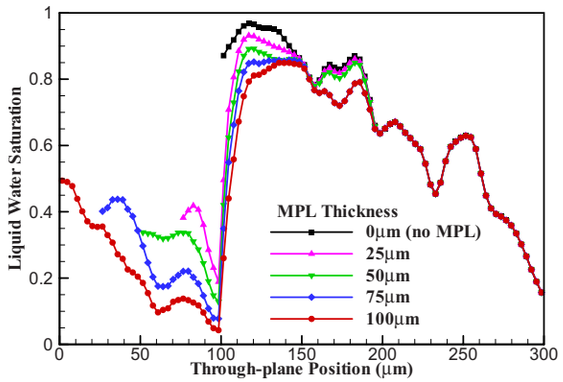

Figure 10. (Color online) Effect of MPL thickness on liquid water saturation.

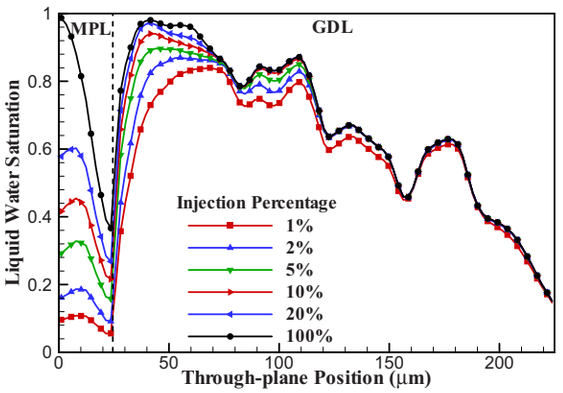

Figure 11. (Color online) Effect of injection percentage on liquid water saturation for MPL thickness of 25 μm.

liquid breakthrough number from the MPL decreases from 75 to 16, whereas the MPL thickness increases from 25 to 100 μm. The liquid breakthrough sites from the upstream porous layer are actually liquid injection sites to the downstream layer. Therefore, the MPL plays its role by reducing the number of liquid water injection sites to the GDL as is achieved through two effects. First, the MPL significantly decreases the liquid injection percentage to the diffusion media, as shown in Table II. Second, the liquid water clusters in the MPL merge into narrower transport paths. The MPL with a larger thickness extends the search of liquid water for its transport paths. Accordingly, more liquid water clusters merges and fewer flooded pores exist before reaching the GDL for the thicker MPL. Despite a saturation jump at the MPL–GDL interface, this sharp increase in saturation does not offset the saturation reduction effect of the MPL. The saturation level in the GDL is still lower than it is without the MPL.

However, the GDL saturation near the channel is less sensitive to the MPL thickness. The saturation levels near the channel (Fig. 10) and the liquid water breakthrough number at the GDL–GC surface (Table III) are almost the same for all MPL thicknesses in the present study. Similar behaviors are also observed in Fig. 9 and 11, where the saturation profiles are quite similar in the GDL downstream region, irrespective of the injection percentage. These behaviors imply that the saturation profiles as well as the liquid water breakthrough (from the GDL) location and number density are more a function of the GDL microstructure than upstream conditions (such as MPL thickness, injection percentages to the MPL, etc.). This finding is attributed to the capillary fingering regime and GDL microstructure characteristics. As shown in Fig. 6, at the beginning of the liquid invasion into the MPL, the three traced clusters (plotted as red, blue, and green) are very small, implying the coexistence of many other liquid clusters. The number of the liquid clusters reduces greatly after the liquid water reaches the GDL, leaving only three major paths in the GDL at the end of invasion. This result suggests that, compared to the MPL, the GDL is characterized by much fewer low resistance paths (major paths) that possess higher priority for liquid water to invade through, owing to the much larger spaces among carbon fibers. Therefore, whatever the liquid water distribution at the MPL–GDL interface, the liquid water invasion paths converge to the major ones with the lowest resistance, leading to similar saturation profiles in the GDL and roughly the same number of liquid droplets emerging from the GDL surface.

Table III. Number of liquid water breakthroughs from MPL and GDL.

MPL thickness (μm)	No. of breakthrough from MPL	No. of breakthrough from GDL
100	16	3
75	26	3
50	41	3
25	75	3
0	89 (from CL)	3

In the preceding section where the effect of current densities is investigated for the 100 μm thick MPL, the MPL breakthrough saturation (the MPL saturation at the MPL–GDL interface) under different injection percentages are low and very close, ranging between 0.019 and 0.039. In this section, to evaluate the effect of MPL thickness on this behavior, a much thinner MPL of 25 μm is used. The saturation profiles at different injection percentages are shown in Fig. 11. For this 25 μm thick MPL, its breakthrough saturation under different injection percentages are much higher and quite distinct from each other, ranging from 0.05 to 0.36. The higher saturation level is a result of more liquid injection sites to the GDL for a thinner MPL. This confirms the effect of the MPL thickness concluded from Fig. 10. Due to the very different breakthrough saturations from the MPL, the GDL saturation levels near the MPL under various injection percentages fall apart, but they soon become very close further downstream. This trend indicates that a thinner MPL possess higher sensitivity of saturation to current density in the composite diffusion layers. However, this sensitivity in the MPL is still much higher than it is in the GDL, owing to the saturation jump that reduces the upstream effects.

Conclusion

Liquid water transport through PEMFC diffusion media composed of an MPL and a GDL is simulated by employing the quasi-static invasion percolation algorithm in a TEPN. The macroscopic saturation distribution along the through-plane direction has been calculated by an improved algorithm.

A sharp saturation increase across a thin interfacial region has been found at the MPL–GDL interface, which confirms the saturation jump predicted by continuum models. A statistical analysis of the pore- and throat-size distributions reveals that the interfacial region is caused by the small GDL pores whose sizes ranges between characteristic sizes of MPL and GDL pores. At pore level, the sharp saturation increase across the interfacial region is a result of the low entry pressure of the GDL and multiple connections of MPL pores to one GDL pore.

The saturation levels at low/high current densities are investigated by changing the liquid breakthrough density from the CL, which is further related to the injection percentages at the MPL inlet surface. The sensitivity of liquid saturation to the injection percentages is high in the MPL but very low in the GDL, indicating that liquid water saturation in the GDL is less affected by the current density if the MPL is added. The influence of current density on saturation profiles decreases as the MPL thickness increases.

The water management role of the MPL is studied by varying its thickness. Adding an MPL or increasing the MPL thickness leads to reduced flooding in the cathode GDL, owing to the decreased number of liquid water injection sites to the GDL, implying less mass transport losses.

The TEPN simulation results indicate a strong influence of the GDL–MPL pore structure on liquid water transport behavior, providing detailed mesoscopic views of water transport processes at the MPL–GDL and GDL–GC interfaces.

Acknowledgments

The financial support of this work by DOE EERE Fuel Cell Technologies Program and ECEC industrial sponsors is gratefully acknowledged.

The Pennsylvania State University assisted in meeting the publication costs of this article.

References

1. D. Spernjak, A. K. Prasad, and S. G. Advani, *J. Power Sources*, **170**, 334 (2007).
2. A. Z. Weber and J. Newman, *J. Electrochem. Soc.*, **152**, A677 (2005).
3. H. Li, Y. H. Tang, Z. W. Wang, Z. Shi, S. H. Wu, D. T. Song, J. L. Zhang, K. Fatih, J. J. Zhang, H. J. Wang, et al., *J. Power Sources*, **178**, 103 (2008).
4. J. H. Nam and M. Kaviany, *Int. J. Heat Mass Transfer*, **46**, 4595 (2003).
5. U. Pasaogullari and C. Y. Wang, *Electrochim. Acta*, **49**, 4359 (2004).
6. U. Pasaogullari, C. Y. Wang, and K. S. Chen, *J. Electrochem. Soc.*, **152**, A1574 (2005).
7. Z. G. Qi and A. Kaufman, *J. Power Sources*, **109**, 227 (2002).
8. G. Y. Lin and T. Van Nguyen, *J. Electrochem. Soc.*, **152**, A1942 (2005).
9. H. K. Atiyeh, K. Karan, B. Peppley, A. Phoenix, E. Halliop, and J. Pharoah, *J. Power Sources*, **170**, 111 (2007).
10. K. Karan, H. Atiyeh, A. Phoenix, E. Halliop, J. Pharoah, and B. Peppley, *Electrochem. Solid-State Lett.*, **10**, B34 (2007).
11. X. H. Wang and T. Van Nguyen, *J. Electrochem. Soc.*, **157**, B496 (2010).
12. V. P. Schulz, J. Becker, A. Wiegmann, P. P. Mukherjee, and C. Y. Wang, *J. Electrochem. Soc.*, **154**, B419 (2007).
13. P. P. Mukherjee, C. Y. Wang, and Q. J. Kang, *Electrochim. Acta*, **54**, 6861 (2009).
14. P. K. Sinha and C. Y. Wang, *Electrochim. Acta*, **52**, 7936 (2007).
15. P. K. Sinha and C. Y. Wang, *Chem. Eng. Sci.*, **63**, 1081 (2008).
16. B. Markicevic, A. Bazylak, and N. Djilali, *J. Power Sources*, **171**, 706 (2007).
17. J. T. Gostick, M. A. Ioannidis, M. W. Fowler, and M. D. Pritzker, *J. Power Sources*, **173**, 277 (2007).
18. K. J. Lee, J. H. Nam, and C. J. Kim, *Electrochim. Acta*, **54**, 1166 (2009).
19. K. J. Lee, J. H. Nam, and C. J. Kim, *J. Power Sources*, **195**, 130 (2010).
20. M. Rebai and M. Prat, *J. Power Sources*, **192**, 534 (2009).
21. L. Ceballos and M. Prat, *J. Power Sources*, **195**, 825 (2010).
22. K. E. Thompson, *AIChE J.*, **48**, 1369 (2002).
23. G. Luo, Y. Ji, C. Y. Wang, and P. K. Sinha, *Electrochim. Acta*, **55**, 5332 (2010).
24. J. T. Gostick, M. A. Ioannidis, M. D. Pritzker, and M. W. Fowler, *J. Electrochem. Soc.*, **157**, B563 (2010).
25. R. Lenormand, E. Touboul, and C. Zarcone, *J. Fluid Mech.*, **189**, 165 (1988).
26. D. Wilkinson and J. F. Willemsen, *J. Phys. A*, **16**, 3365 (1983).
27. F. Y. Zhang, X. G. Yang, and C. Y. Wang, *J. Electrochem. Soc.*, **153**, A225 (2006).
28. G. Mason and N. R. Morrow, *J. Colloid Interface Sci.*, **141**, 262 (1991).
29. J. H. Nam, K. J. Lee, G. S. Hwang, C. J. Kim, and M. Kaviany, *Int. J. Heat Mass Transfer*, **52**, 2779 (2009).
30. K. Broka and P. Ekdunge, *J. Appl. Electrochem.*, **27**, 281 (1997).
31. F. Y. Zhang, D. Spernjak, A. K. Prasad, and S. G. Advani, *J. Electrochem. Soc.*, **154**, B1152 (2007).
32. C. Hartnig, I. Manke, R. Kuhn, N. Kardjilov, J. Banhart, and W. Lehnert, *Appl. Phys. Lett.*, **92**, 134106 (2008).
33. M. A. Hickner, N. P. Siegel, K. S. Chen, D. S. Hussey, D. L. Jacobson, and M. Arif, *J. Electrochem. Soc.*, **155**, B427 (2008).